Research Article

Facile synthesis and antibacterial applications of cuprous oxide/bovine serum albumin hierarchical nanocomposite particles

Shuyan Zhao[1] · Yujie Gao[1] · Jinhui Tan[2] · Yuntao Zhu[2] · Xiaohong Ying[2] · Mengmeng Zhang[2] · Xufeng Yu[2] · Bo You[1]

Abstract
A facile method to prepare cuprous oxide/bovine serum albumin (Cu_2O/BSA) hierarchical nanocomposite particles (NCPs) through imitating biomineralization is presented. BSA acted as the structure-directing agents, guiding the nucleation, growth and assembly of $Cu(OH)_2$ at binding sites to construct the hierarchical structure and then Cu_2O/BSA NCPs were achieved. The synthesized nanocomposite with hierarchical structure exhibited excellent antibacterial performance. The products obtained were characterized with XRD, TEM, FTIR, EDX and XPS to investigate the formation mechanism of Cu_2O/BSA hierarchical structure. Cu_2O/BSA NCPs with size of 20–50 nm built up by several 6–7 nm Cu_2O nanocrystals with BSA showed better antibacterial performance in the comparative experiments, which was attributed to the special structure and good biocompatibility of the Cu_2O/BSA NCPs. And the possible mechanism was presented to explain the excellent antibacterial properties of Cu_2O/BSA NCPs.

Keywords Biomineralization · Cuprous oxide · Bovine serum albumin · Hierarchical nanocomposite particles · Antibacterial

1 Introduction

In nature, biological systems can control the nucleation, growth and assembly of crystals precisely and efficiently by biomineralization [1]. Many kinds of crystals with specific shape and size can be obtained [2]. Therefore, biomineralization has attracted the attentions of many researchers. Numerous kinds of biomolecules and organic matrixes have been used as templates to simulate the biomineralization process during the synthesis of functional materials [3–6]. Bovine serum albumin (BSA) is a common and commercially available protein with good solubility and biocompatibility. BSA is available to interact with a variety of metal ions as a biomacromolecule with various functional groups, such as amino and carboxyl groups. Thus, it is often used as structure-directing reagents during the biomineralization process. Xie et al. [7] synthesized gold nanoclusters consisted of 25 gold atoms by BSA. The structure showed good stability, biocompatibility and high quantum yield. Yilmaz et al. [8] prepared BSA–Cu(II) hybrid nanoflowers by biomineralization and the products were successfully used as absorbent for solid phase extraction. SiO_2 nanoparticles were modified with BSA by Mallakpour et al. [9]. The modified SiO_2–BSA nanoparticles had good dispersion in PVC matrix and the achieved nanocomposite film were improved in the optical, mechanical and thermal characteristics. The grain size and special structure of synthetic materials can be controlled effectively by using BSA as the structure-directing

Electronic supplementary material The online version of this article (https://doi.org/10.1007/s42452-019-0963-9) contains supplementary material, which is available to authorized users.

✉ Bo You, youbo@fudan.edu.cn | [1]Department of Materials Science and the Advanced Coatings Research Center of Ministry of Education of China, Fudan University, Shanghai 200433, People's Republic of China. [2]Zhejiang Academy of Science and Technology for Inspection and Quarantine (Jiaxing), Jiaxing 314000, Zhejiang, People's Republic of China.

Received: 19 April 2019 / Accepted: 20 July 2019 / Published online: 25 July 2019

reagent. In addition, the obtained materials exhibit good stability and compatibility.

Cuprous oxide (Cu_2O) is a semiconductor material with good redox and photoelectric properties. Therefore, it has broad applications in catalysts, water splitting, antifouling, gas sensing and solar cells [10–14]. Copper owns lower toxicity and cost, so Cu_2O is often used as an antibacterial agent [15–17]. In order to improve the antibacterial properties of Cu_2O, a lot of studies has been carried out. Some researchers controlled the shape and morphology of Cu_2O to enhance antibacterial activity [18, 19]. Wang et al. [20] synthesized Cu_2O octahedrons, cubes, hollow spheres and flowers, and the hierarchical flowerlike microstructures consisted of nanosheets displayed the best antibacterial property. Some researchers added other materials (such as Ag and TiO_2) and fabricated composites with specific structures [21, 22]. The added materials might play the synergism with Cu_2O to improve the antibacterial performance. However, most researchers took only one of these two methods to improve antibacterial properties of Cu_2O.

Because of the high accuracy and efficiency of biomineralization, some biomolecules have been used as capping and stabilizing agents during the synthesis of Cu_2O [23, 24]. However, the structure-directing mechanism was not studied in detail in the previous researches. Moreover, the effects of biomolecules during the synthesis process were discussed but the functions of biomolecules in the antibacterial process failed to be considered.

In this work, a novel synthesis of cuprous oxide/bovine serum albumin (Cu_2O/BSA) hierarchical nanocomposite particles (NCPs) with size of 20–50 nm built up by several 6–7 nm Cu_2O nanocrystals and BSA is reported. Furthermore, a possible mechanism of the nucleation, growth and assembly of Cu_2O/BSA NCPs is provided. A hierarchical structure is the higher dimensional structure composed of low dimensional nanomaterials [25]. The designed hierarchical structure possesses both the properties of the primary and secondary structures [26]. Therefore, the Cu_2O/BSA hierarchical structure exhibited excellent antibacterial performance which was due to the combination of the special Cu_2O/BSA hierarchical structure and good biocompatibility of BSA.

2 Experimental section

2.1 Materials

Copper acetate ($Cu(Ac)_2{\cdot}H_2O$), sodium hydroxide (NaOH), ascorbic acid, cuprous oxide (Cu_2O), potassium dihydrogen phosphate (KH_2PO_4) were purchased from Guoyao Chemical Reagent Co (China). Bovine serum albumin (BSA, 96 wt%), cuprous chloride (CuCl) were purchased from Shanghai Aladdin Biochemical Technology Co (China). Ethanol was purchased from Shanghai Titan Scientific Co (China). All chemicals were analytical-grade regents and used without further purification. *Staphylococcus aureus* ATCC 25923 (*S. aureus*) and *Escherichia coli* ATCC 25922 (*E. coli*) were supplied by Jiaxing Entry-Exit Inspection and Quarantine Bureau (China). Nutrient broth, nutrient agar, defiber sheep blood, Baird-Parker medium base (CM302) and GCM105 eosin methylene blue agar (EMB) were purchased from Beijing Land Bridge Technology Co (China).

2.2 Synthesis of Cu_2O/BSA NCPs

A certain amount of BSA (0.1 g, 0.2 g, 0.3 g and 0.4 g) was dissolved in 54 g of distilled water at 37 °C under stirring. 0.1 g $Cu(Ac)_2{\cdot}H_2O$ was dissolved in 60 g of distilled water and then the solution was added into the above BSA solution under vigorous stirring. The solution changed to white. After mixed for 10 min, 2 mL NaOH (1 mol L^{-1}) was added and purple solution was obtained. Then 0.2 g ascorbic acid was dissolved in 4 g of distilled water and added into the above purple solution to reduce Cu(II) to Cu(I). The color of solution became yellow gradually. The mixed solution was stirred at 37 °C for different time (1 min, 10 min, 30 min, and 60 min) and the Cu_2O/BSA NCPs dispersion was achieved. Finally, the Cu_2O/BSA NCPs sample was collected and washed several times with distilled water and ethanol and then dried for 24 h. Meanwhile, Cu_2O samples without the addition of BSA (BSA-0–Cu_2O) were prepared for comparing. The samples produced under different conditions were showed in Table 1. All the experimental steps of the other samples were consistent with the synthetic process of Cu_2O/BSA NCPs.

2.3 Antibacterial performance test

34.0 g of KH_2PO_4 and 500 mL distilled water were mixed and then the pH was adjusted by 175 mL of NaOH (1 mol L^{-1}). The mixed solution was subsequently diluted to 1000 mL with distilled water. 1.25 mL of above solution

Table 1 Samples of Cu_2O/BSA NCPs produced under different conditions

Sample	Reaction time (min)	Amount of BSA (g)
BSA–Cu_2O-1	1	0.2
BSA-0–Cu_2O	60	0
BSA-0.1–Cu_2O	60	0.1
BSA–Cu_2O	60	0.2
BSA-0.3–Cu_2O	60	0.3
BSA-0.4–Cu_2O	60	0.4

was further diluted to 1000 mL with distilled water and autoclaved to obtain phosphate buffer solution (PBS). *S. aureus* and *E. coli* were activated on blood agar and cultivated in nutrient broth.

Equivalent BSA-0–Cu_2O, BSA–Cu_2O, commercial Cu_2O and CuCl were added to PBS containing equivalent *S. aureus* and *E. coli* separately to test the antimicrobial properties of different samples. The final concentration of sample was 10 μg mL^{-1} and that of bacteria was 10^6 CFU mL^{-1}. Different solutions above were placed in orbital shaker at 37 °C for different durations. And then 100 μL of *S. aureus* and *E. coli* reaction solution were plated on CM302 and EMB agar plates, respectively, and incubated at 37 °C for 24 h to obtain plate counting. Each group was repeated for three times.

Different samples were dissolved in PBS solution which is similar with antimicrobial tests but without bacteria and the samples were shook in the orbital shaker for copper release studies. The concentrations of ion release for different durations were measured by ICP-AES.

2.4 Characterization

Transmission electron microscopy (TEM) was performed on a FEI Tecnai G2 20 TWIN microscope. Field-emission scanning electron microscopy (FESEM) and energy dispersive X-ray (EDX) were obtained on a Zeiss Ultra 55 field-emission scanning electron microscope. High-resolution transmission electron microscopy (HRTEM) and select-area electron diffraction (SAED) were measured on a JEOL JEM-2010 microscope. Powder X-ray diffraction (XRD) was tested on a Bruker D8A Advance. Fourier transform infrared spectroscopy (FTIR) was achieved on a Thermo Fisher Nicolet Nexus 470 infrared spectrometer. The X-ray photoelectron spectroscopy (XPS) was characterized on a Perkin-Elmer PHI 5000C ECSA instrument. Fluorescence spectroscopy was measured by a PTI QM 40 spectrometer with excitation wavelength of 278 nm. Circular dichroism (CD) was operated on a Bio-Logic MOS-450 spectrometer. Inductively coupled Plasma-atomic emission spectroscopy (ICP-AES) was performed on Hitachi P-4010.

3 Results and discussion

3.1 Structure and morphology

The XRD analysis of the products obtained under different conditions was shown in Fig. 1. For BSA, there was a characteristic peak of organics at around 22° (Fig. 1a). The observed characteristic peak indicated the existence of BSA when the reaction time was 1 min (Fig. 1b). And three diffraction peaks at 36.7°, 42.4° and 62.2° appeared

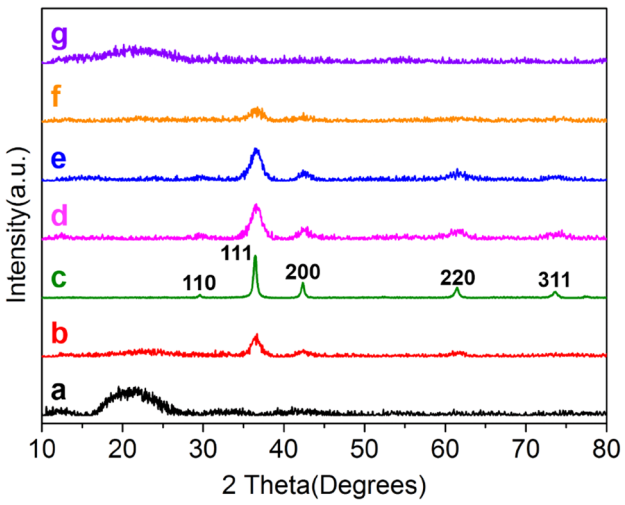

Fig. 1 XRD patterns of BSA and Cu_2O/BSA NCPs samples obtained under different conditions: (a) BSA, (b) BSA–Cu_2O-1, (c) BSA-0–Cu_2O, (d) BSA-0.1–Cu_2O, (e) BSA–Cu_2O, (f) BSA-0.3–Cu_2O, (g) BSA-0.4–Cu_2O

in Fig. 1b which matched Cu_2O (JCPDS 65-3288) and represented (111), (200) and (220) planes of Cu_2O. It suggested that Cu_2O could be synthesized rapidly. The intensity of diffraction peaks (Fig. 1e) gradually increased as the reaction time prolonged, implying the increase of crystallinity degree. The samples with different content of BSA were compared when the reaction time reached 1 h. Five obvious diffraction peaks were found in BSA-0–Cu_2O (Fig. 1c) and the marked diffraction peaks all matched Cu_2O (JCPDS 65-3288). The average grain size was 36 nm according to the calculation of the XRD results. BSA-0.1–Cu_2O (Fig. 1d) and BSA–Cu_2O (Fig. 1e) also showed five diffraction peaks of Cu_2O without other impurities, but the peak width was larger, indicating the smaller grain size. The average grain sizes were 4.0 and 6.4 nm, respectively. This demonstrated that the addition of BSA could reduce the grain size of Cu_2O significantly. The intensities of Cu_2O diffraction peak decreased as the content of BSA further increased. Only two diffraction peaks of Cu_2O could be observed in BSA-0.3–Cu_2O (Fig. 1f) and only the peak of BSA could be seen when the BSA increased to 0.4 g (Fig. 1g), indicating that excessive BSA might reduce the content of Cu_2O and make the formation of Cu_2O tougher. Therefore, the addition of BSA was better to be controlled in the range of 0.1–0.2 g.

To investigate the composition of the Cu_2O/BSA hierarchical structure, the element contents of the sample BSA–Cu_2O and pure BSA were compared by EDX and XPS (Table 2). The main components of BSA are C, N, O, P, S, and Cu_2O includes element Cu and O. Both results showed that BSA–Cu_2O also contained C, N, P and S elements besides Cu and O elements, which suggested that BSA–Cu_2O contained a large number of organics. The proportions of

Table 2 EDX and XPS element contents (at%) of BSA and BSA–Cu_2O

Characterization	Sample	C	N	O	P	S	Cu
EDX	BSA	71.64	11.91	15.61	0.03	0.82	0
	BSA–Cu_2O	62.70	7.69	14.02	0.02	0.43	15.14
XPS	BSA	70.07	9.95	19.29	0.08	0.61	0
	BSA–Cu_2O	68.45	7.73	22.07	0.10	0.51	1.41

elements in BSA–Cu_2O were similar with pure BSA. Thus, BSA–Cu_2O was composite materials, which contained both BSA and Cu_2O. In addition, the contents of Cu tested by two kinds of characterization methods were quite different. EDX can measure the elements of bulks and the testing depth reaches micron level, while XPS can only test the element contents of surface and the depth is nanoscale. Therefore, it proved that the Cu_2O was more likely to locate in the internal of samples and BSA tended to distribute on the surface of samples, suggested that Cu2O and BSA dispersed from each other in the hierarchical structure.

Figure 2 presented the morphology of samples obtained under different conditions. There were many nanoparticles with the particle size of 20 to 50 nm in Cu_2O without BSA (Fig. 2a), while the sample had no porous structure. Figure 2b showed the morphology of BSA–Cu_2O-1. Many nanocomposite particles with porous structure and particle size of 20 to 50 nm could be observed. These NCPs were surrounded by organic films. The TEM images of Cu_2O/BSA NCPs obtained with different reaction time are shown in Fig. S1. The homogeneity and dispersibility of Cu_2O/BSA NCPs are getting better as time increases. Combined with the XRD results, it illustrated that the Cu_2O formed rapidly and the specific morphology of Cu_2O/BSA NCPs formed after only 1 min. The morphology stabilized after reacting 1 h, so 1 h was chosen to be the reaction time. The morphology of samples prepared by adding different contents of BSA was different. The particle size was similar but porous structures appeared when adding 0.1 g BSA (Fig. 2c). And there was a slight agglomeration between nanoparticles. When the addition of BSA increased to 0.2 g (Fig. 2d), the morphology of the nanocomposites was similar with that of BSA-0.1–Cu_2O. However, BSA–Cu_2O had better dispersion

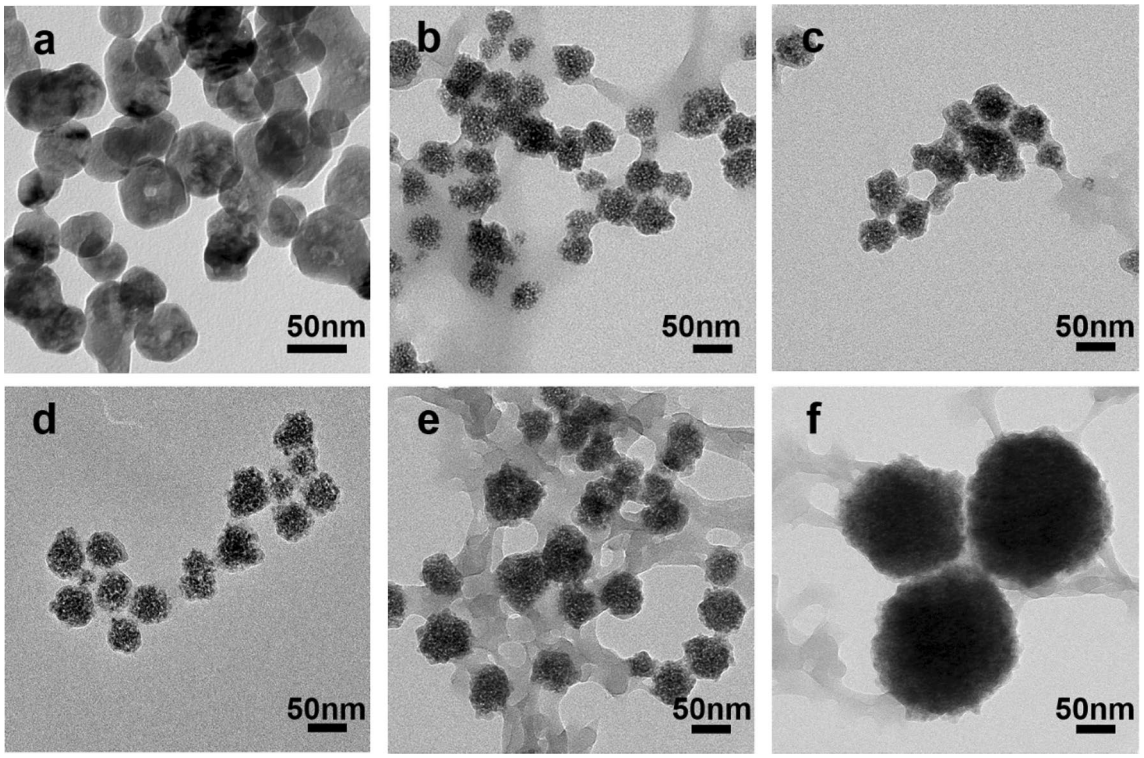

Fig. 2 TEM images of Cu_2O/BSA NCPs obtained under different conditions: **a** BSA-0–Cu_2O, **b** BSA–Cu_2O-1, **c** BSA-0.1–Cu_2O, **d** BSA–Cu_2O, **e** BSA-0.3–Cu_2O, **f** BSA-0.4–Cu_2O

and less aggregation. Lots of organic films were observed when BSA increased to 0.3 g (Fig. 2e). In this sample, the porous structure was still reserved, but the particle size was slightly larger than that of BSA–Cu_2O. When the BSA content increased to 0.4 g (Fig. 2f), besides the more organic films, the particle size exceeded 100 nm and the porous structure disappeared. Unlike BSA-0–Cu_2O, BSA-0.4–Cu_2O had rough surface. The figure showed the existence of Cu_2O in this scale, but the overall content was quite low. Actually, most of the samples were organic films which were consistent with the XRD results. Thus, the content of BSA was determined to be 0.2 g.

The structures of BSA–Cu_2O were analyzed by HRTEM as shown in Fig. 3. Figure 3a showed the structure of the sample BSA–Cu_2O: Cu_2O crystals were mixed with organics (BSA), which was consistent with the results of EDX and XPS. Figure 3b exhibited the structure of single BSA–Cu_2O nanoparticle. It could be seen that the nanoparticle was assembled by several smaller sub-nanocrystals. Figure 3c showed the HRTEM image of single BSA–Cu_2O nanoparticle. There were several lattice fringes in different directions indicating the existence of the polycrystalline structure. So nanocomposite could be divided into small sub-nanocrystal, based on the lattice fringe direction and contrast of images, as shown in white dotted line circle of Fig. 3c. It seemed that the nanocrystal size was about 7 nm, which was consistent with the XRD calculation. And the spacing between adjacent lattice planes was about 0.25 nm, which corresponded to the distance of Cu_2O (111) planes. Figure 3d presented the SAED pattern of BSA–Cu_2O nanoparticles. There were five diffraction rings, corresponded to the (110), (111), (200), (220) and (311) crystal planes of Cu_2O. There were no other diffraction rings, suggesting that BSA–Cu_2O contained only Cu_2O, but no other impurities such as Cu and CuO.

3.2 Mechanism analysis

The FTIR spectra of different samples were shown in Fig. 4. For pure BSA (Fig. 4a), a broad band attributed to the stretching vibration of O–H and N–H groups appeared at around 3306 cm^{-1}. The stretching vibration of C=O was at 1657 cm^{-1}. The characteristic band at 1541 cm^{-1} was assigned to the stretching vibration of C–N and bending vibration of N–H [27]. The band of 1395 cm^{-1} belonged to the bending vibration of C–H. Figure 4e showed the FTIR spectrum of commercial Cu_2O. There was only one band at 629 cm^{-1} that was corresponded to the Cu–O group. The band of Cu–O had appeared when the reaction time was 1 min (Fig. 4b), indicating the existence of Cu_2O. Compared

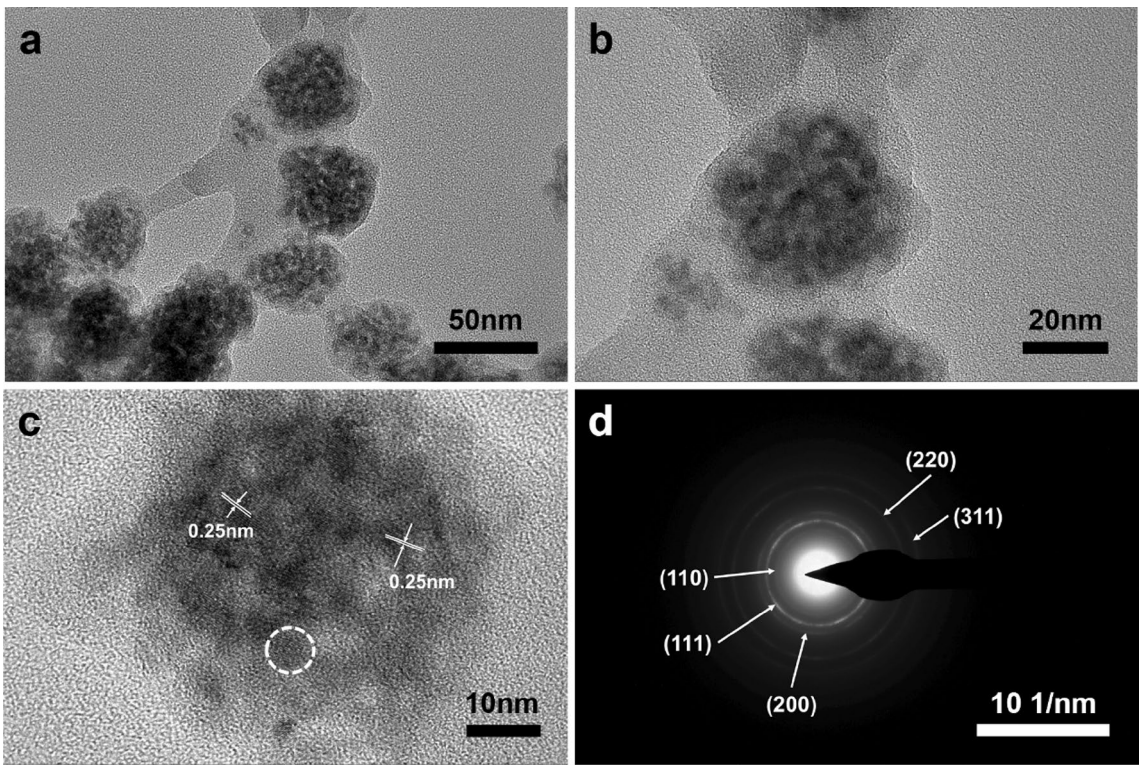

Fig. 3 **a** TEM image of the sample BSA–Cu_2O, **b** TEM image of the single BSA–Cu_2O nanoparticle, **c** HRTEM lattice image of BSA–Cu_2O nanoparticles, **d** the SAED pattern of **b**. One single nanocrystal is within a white dotted line circle

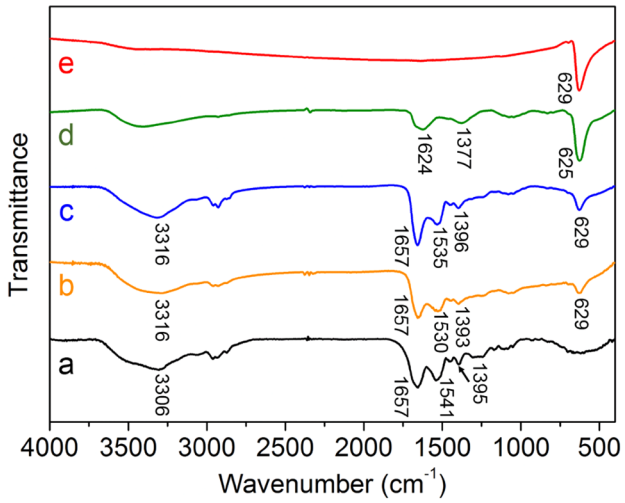

Fig. 4 FTIR spectra of: (a) BSA, (b) BSA–Cu_2O-1, (c) BSA–Cu_2O, (d) BSA-0–Cu_2O, (e) commercial Cu_2O

with pure BSA, the sample had all functional groups of BSA suggesting that the presence of BSA. In addition, the stretching vibration of C=O did not shift which meant the carbonyl group did not interact with Cu^{2+}. However, the vibration band of C–N and N–H shifted to lower wavenumber, which was due to the coordination of Cu^{2+} with N atoms. The FTIR spectrum of BSA–Cu_2O (Fig. 4c) was similar with that of BSA–Cu_2O-1. There were also some organic functional groups besides the Cu–O bond in BSA-0–Cu_2O (Fig. 4d). This might be owing to some groups of residual ascorbic acid.

Pure BSA and BSA–Cu_2O were tested by XPS to explore the coordination of functional groups with Cu^{2+}, and the results were shown in Fig. 5. Figure 5a showed the general XPS of pure BSA and BSA–Cu_2O. Detailed data and analysis could be seen in Table 2.

Figure 5b presented the O 1*s* XPS of BSA and BSA–Cu_2O. For pure BSA, the peaks located at 530.9 and 532.4 eV were attributed to C=O and O–H bonds, respectively [27]. For BSA–Cu_2O, these two peaks slightly shifted to 531.0 and 532.5 eV, respectively. Combined with the FTIR results,

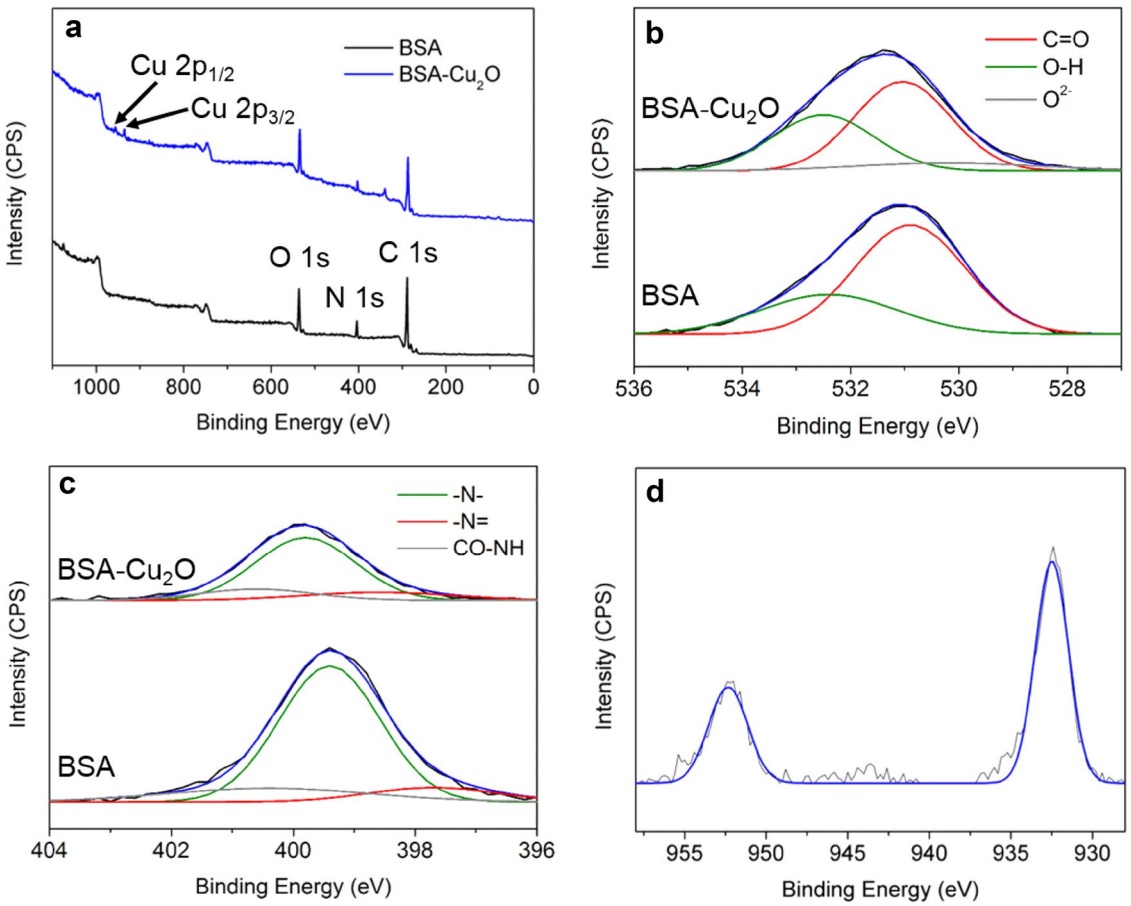

Fig. 5 **a** The general XPS spectra, **b** O 1*s* XPS spectra, **c** N 1*s* XPS spectra of the samples BSA and BSA–Cu_2O, **d** Cu 2*p* XPS spectra of the sample BSA–Cu_2O

C=O and O–H might have coordination with Cu^{2+}, but the bond was weak compared to other groups. Besides, a new peak at 530.2 eV appeared corresponding to the O^{2-} ions in the Cu_2O lattice, indicating the formation of Cu_2O [28].

Figure 5c presented the N 1*s* XPS of BSA and BSA–Cu_2O. For pure BSA, the peaks located at 397.7, 399.4 and 400.4 eV were due to imine, amine and amide bonds, respectively [29]. For BSA–Cu_2O, the intensity of N 1*s* reduced and the three peaks shifted to 398.6, 399.8 and 400.6 eV, respectively, indicating that the electron density of N atoms was less than that in BSA. It illustrated that N atoms all had coordination with Cu ions, which was consistent with the FTIR results. The imine bond shifted the most. Histidine has imine bond among amino acids, which indicated that N atoms of the histidine residues in BSA had stronger coordination with Cu^{2+}. And lysine, arginine and tryptophan have amine bond on the side chains, implying that N atoms of these residues participated in the coordination. Glutamine and asparagine have amide structures. Since the shift was small, the coordination of these residues was relatively weak.

Figure 5d presented the Cu 2*p* XPS of BSA and BSA–Cu_2O. The peaks located at 932.5 and 952.3 eV were due to Cu $2p_{3/2}$ and Cu $2p_{1/2}$, respectively [30]. No other Cu 2*p* peaks were observed, indicating that there were no other impurities, such as Cu or CuO.

Pure BSA has a large fluorescence peak at 300–460 nm, indicating the intact structure of the fluorescent group such as tryptophan in BSA. In the sample BSA–Cu_2O, the fluorescence peak disappears completely and fluorescence quenching occurred, for that these fluorophore-containing amino acid residues coordinate with Cu^{2+}, and the fluorescence intensity is greatly reduced to zero. In our research, the binding of the groups in BSA to Cu^{2+} is investigated through observing the change of the peak at 300–460 nm. Circular dichroism spectra (CD) are widely applied to determine the secondary structure of protein for studying the conformation of proteins. CD spectra were used to investigate the structural changes of BSA before and after the reaction, to support the formation mechanism of Cu_2O/BSA NCPs. To explore the changes of BSA during the reaction, the fluorescence and CD spectra of the samples BSA and BSA–Cu_2O were shown in Fig. 6.

Figure 6a exhibited the fluorescence spectra of the two samples excited at 278 nm [31]. BSA had a significant fluorescence due to the tryptophan residues [31]. For BSA–Cu_2O, the fluorescence was quenched, indicating the destruction of the residues. Combined with the XPS results, it demonstrated the coordination of indole amine in tryptophan residues with Cu^{2+}. Figure 6b showed the CD spectra of BSA and BSA–Cu_2O. For pure BSA, there was a band at 222 nm which was the characteristic transition of α-helical structure of BSA [32]. However, the negative band of BSA–Cu_2O completely disappeared. It was the coordination of Cu^{2+} and BSA that broke the hydrogen bond which was located in the α-helical structure and destroyed the secondary structure of BSA. Finally, the chains of the α-helical region were stretched.

Based on the investigations and results above, a possible formation mechanism of Cu_2O/BSA NCPs is presented in Fig. 7. Figure 7a showed the structure of BSA. Based on the results above, the tryptophan and histidine residues had stronger coordination with Cu^{2+} while that of the other functional groups on side chain was weaker. Thus, the former was the major consideration on the formation mechanism. One BSA molecule has 2 tryptophan residues and 17 histidine residues [33]. The locations of one tryptophan and one histidine residues were marked in the Fig. 7a. Theoretically, they could all coordinate with Cu^{2+}. However, there was a strong binding site at the N-terminal tetrapeptide (Asp–Thr–His–Lys) and Cu^{2+} would first coordinate with this binding site [34]. This step

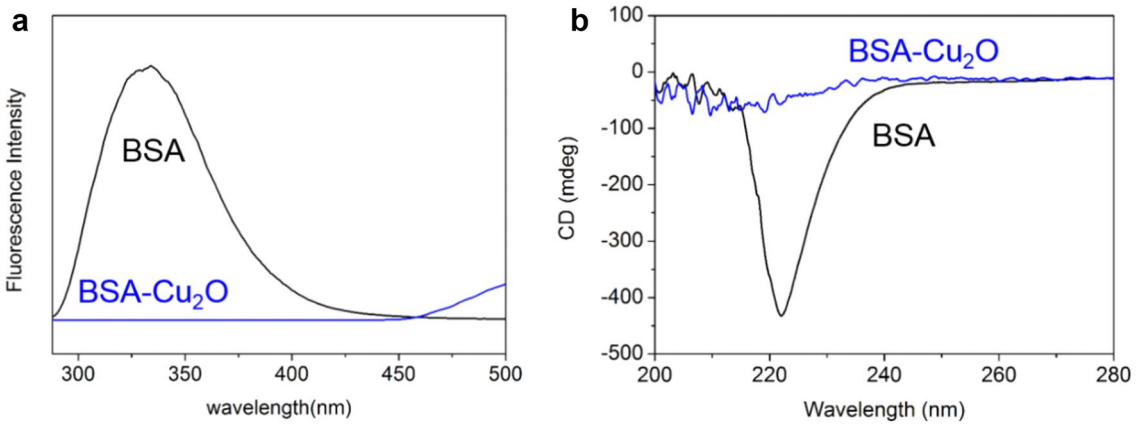

Fig. 6 **a** Fluorescence spectra of the two samples excited at 278 nm, **b** CD spectra of the samples BSA and BSA–Cu_2O

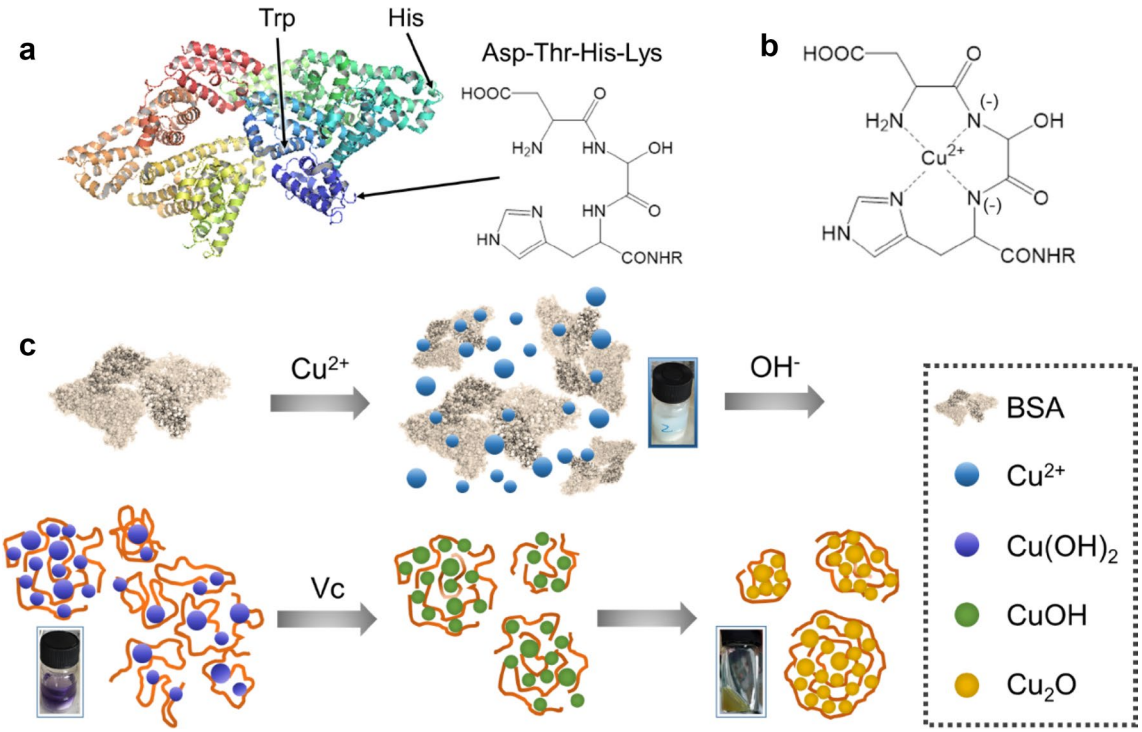

Fig. 7 Schematic illustration of Cu_2O/BSA NCPs formation process: **a** the structure of BSA, **b** N-terminal of BSA binding with Cu^{2+}, **c** formation illustration of the Cu_2O/BSA NCPs

was difficult, but after the first coordination with Cu^{2+}, the conformation of BSA changed. The allosteric effect could inhibit the Cu^{2+}-induced cross-linking of BSA and exposed more binding sites [34]. These both promoted the next coordination of other sites with Cu^{2+}. Figure 7b showed the coordination structure of Cu^{2+} and Asp–Thr–His–Lys under alkaline conditions [35]. The characteristic square planar Cu^{2+} coordinated with the deprotonated amide of Thr and His, amine of Asp and imidazole of His. The reaction was similar with the biuret reaction and the purple Cu complex was formed.

Figure 7c was the formation illustration of Cu_2O/BSA NCPs. Cu^{2+} first coordinated with N-terminal of BSA and changed the protein conformation. Then, the rest of Cu^{2+} could further coordinate with other histidine and tryptophan residues, resulting in the denaturation of BSA and formation of white floc (Figs. S2a and S2d). The N-terminal Cu complex was formed (Fig. 7b) and the solution turned purple after the addition of NaOH. The local concentration of Cu^{2+} at binding sites was quite high, for that the precipitation provided surfaces, which were more likely to adsorb metal ions. Therefore, it was favorable for the extremely rapid reaction of Cu^{2+} with OH^- to generate small $Cu(OH)_2$ precipitates (Fig. S2b). These $Cu(OH)_2$ could grow along the peptide chain of BSA and the structure of BSA changed to porous structure (Fig. S2e). There was certain steric effect around $Cu(OH)_2$ precipitates because of the interspaces between sites and sites and the existence of other amino acid residues and peptide chains. Therefore, the aggregation of $Cu(OH)_2$ was limited and the particle size was controlled in several nanometers. And then the $Cu(OH)_2$ precipitates at the binding sites and BSA assembled together to form a hierarchical structure. BSA was used as the structure-directing agent to guide the nucleation, growth and assembly $Cu(OH)_2$. After ascorbic acid added, the $Cu(OH)_2$ was reduced to CuOH and decomposed into yellow Cu_2O (Fig. S2c). Finally, Cu_2O/BSA NCPs composed of several Cu_2O nanocrystals and BSA were obtained (Fig. S2f).

The whole reaction was very fast and the reaction progress could be judged by the color change. The relative contents of Cu^{2+} and BSA was very important owing to the coordination priority and order as discussed above. Cu^{2+} was not enough for the conformational changes of all the BSA if too much BSA (e.g. 0.4 g) was added. Cu^{2+} could only react with N-terminal of BSA. Moreover, the high protein concentration would hinder the uniform distribution of Cu^{2+}. The α-helical structure would not expand to provide redundant sites, so the steric effect lacked during the formation of $Cu(OH)_2$. Therefore, $Cu(OH)_2$ precipitation was easy to aggregate to form large particles. And numerous Cu^{2+} would be concentrated at N-terminal binding sites, leading to the rapid generation of large amounts of $Cu(OH)_2$ precipitation. Thus, the particle size was even

larger than that of the Cu_2O produced without BSA. The obstruction of protein among the Cu_2O particles was insufficient when the content of BSA was low, so there would be a slight agglomeration.

3.3 Antibacterial performance

Preliminary antibacterial tests against *S. aureus* of BSA-0.1–Cu_2O, BSA–Cu_2O, BSA-0.3–Cu_2O and BSA-0.4–Cu_2O were carried out. The corresponding antibacterial ratio were 95%, 100%, 98% and 88%, respectively. Therefore, BSA–Cu_2O was selected in the following antimicrobial experiments.

To study the antibacterial properties of BSA–Cu_2O, *S. aureus* (gram-positive bacteria) and *E. coli* (gram-negative bacteria) were selected as experimental objects. The antibacterial effect was measured after 60 min reaction and compared with BSA-0–Cu_2O, commercial Cu_2O and CuCl (Fig. S2). The concentration of survival bacteria of the control groups reached 10^5 CFU mL^{-1} for *S. aureus* (Fig. 8a). All survival amounts dropped sharply after different samples added. In BSA–Cu_2O and CuCl groups, no bacteria survive. The survival concentration of BSA-0–Cu_2O and commercial Cu_2O groups were reduced to 10^1 CFU mL^{-1}. The amount of the control groups was also up to 10^5 CFU mL^{-1} for *E. coli* (Fig. 8b). After different samples added, all survival amounts decreased but the overall antibacterial effect was weaker. The reason might be that thinner single-layer and negative phosphate cell wall of gram-positive bacteria made Cu^+ easier to permeate cell walls through electrostatic interactions. The count of commercial Cu_2O group was nearly the same as that of the control group. The number of bacteria in BSA-0–Cu_2O group only decreased one order of magnitude. CuCl group still had 10^1 CFU mL^{-1} of bacteria surviving. However, there were no bacteria existing in BSA–Cu_2O groups. These two experiments indicated that BSA–Cu_2O had better antibacterial properties than the others.

The antibacterial mechanism of Cu_2O is mainly by contacting cell walls to kill bacteria. There are two ways: (1) direct contact with the cell wall of bacteria and damage them, (2) releasing Cu^+ into solution and react with cell walls [36, 37]. In this research, *S. aureus* was used as antibacterial objects to explore the antibacterial mechanism of BSA–Cu_2O. The number of bacteria living and the release amount of copper ions of different samples in different time were investigated.

Figure 9a showed the survival amount of *S. aureus* in different time. The number of living bacteria of Cu_2O group gradually decreased. The decline tend of BSA-0–Cu_2O group was rapid at first and then became slower. The concentration of bacteria in BSA–Cu_2O and CuCl groups decreased very fast. The CuCl group took 10 min to kill all bacteria, while the BSA–Cu_2O group cost only 5 min.

Figure 9b exhibited the copper release of different samples in different time. The cuprous ions of CuCl dissolved in solution and kept high Cu element concentration. The copper release of commercial Cu_2O was slow and stable. BSA-0–Cu_2O released copper rapidly at first and then slowly. The ion release of BSA–Cu_2O was relatively stable. In theory, the release rate should be the fastest due to the large specific surface area of the particles with small size. However, the measured concentration was slightly lower than that of BSA-0–Cu_2O and commercial Cu_2O. This might be attributed to that BSA–Cu_2O contained a certain amount of BSA, and the Cu_2O content was lower than others.

By comparison, the antibacterial velocities of BSA-0–Cu_2O, commercial Cu_2O and CuCl were proportional to the copper release rates. The Cu concentration of CuCl was the highest, so the antibacterial rate was the fastest. The release amount of BSA-0–Cu_2O and commercial

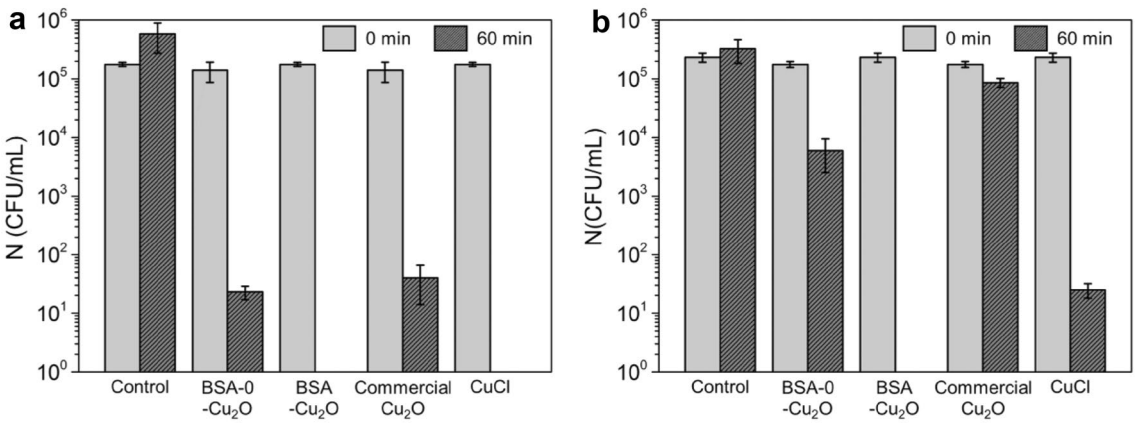

Fig. 8 Survival of **a** *S. aureus*, **b** *E. coli* by using different samples after 60 min of antibacterial action

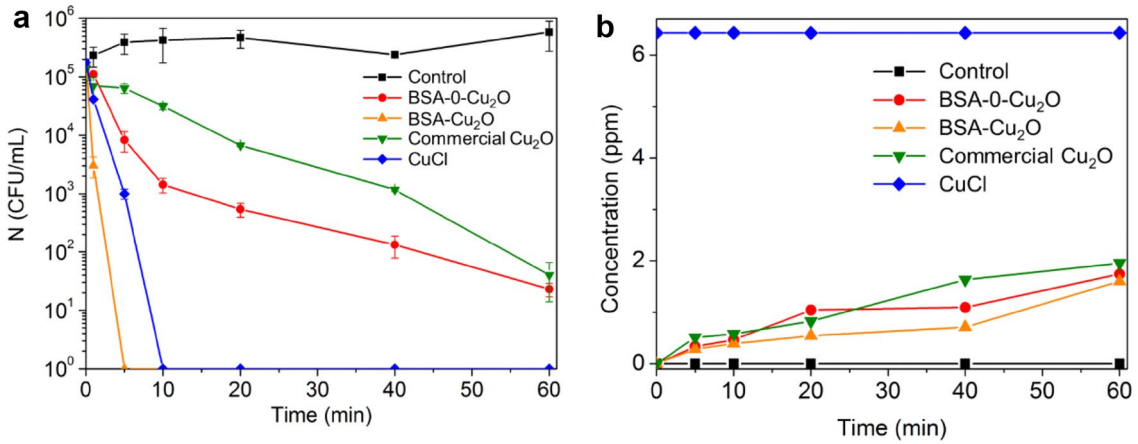

Fig. 9 **a** Survival of *S. aureus* and **b** copper release curves by using different samples in different antibacterial action time

Cu_2O was similar, but the release rate was different. Figure S4 showed the FESEM images and XRD pattern of commercial Cu_2O. There were large numbers of nanoparticles and micro-sized particles in images indicating the particle size distribution was wide. And the narrow diffraction peaks in XRD spectra stated the particle size was quite large. However, the particle size of BSA-0–Cu_2O was much smaller indicating the larger surface area. It could accelerate the Cu release and increase the contact probability with bacteria, so the antibacterial effect was slightly better than that of commercial Cu_2O. For BSA–Cu_2O, the antibacterial effect did not completely depend on the Cu release rate. The release concentration of Cu in BSA–Cu_2O was much less than CuCl, but the antibacterial rate was faster than CuCl, which suggested that direct contact played an important role in antibacterial performance.

Figure 10a, e showed the morphology of *E. coli* and *S. aureus*, and Fig. 10b, f showed the morphology of bacteria after BSA–Cu_2O was added. The bacteria were surrounded by a lot of nanoparticles. And as shown in the insets, the bacteria displayed obvious deformation and the cell walls were destroyed. These both proved that BSA–Cu_2O NCPs contacted with bacteria and reacted with cell walls. According to the elemental mapping of EDX (Fig. 10c, d, g, h), these nanoparticles were containing dispersed Cu and C elements. Therefore, it could be speculated that BSA and Cu_2O were intertwined to construct the BSA–Cu_2O nanocomposite and various amino acid residues distributed in and on the surface of the composite. These residues had good biocompatibility, which was in favor of the direct contact between BSA–Cu_2O nanoparticles and bacterial cell walls, and then BSA–Cu_2O efficiently released copper ions at the fixed point. The Cu^+ ion release mechanism in

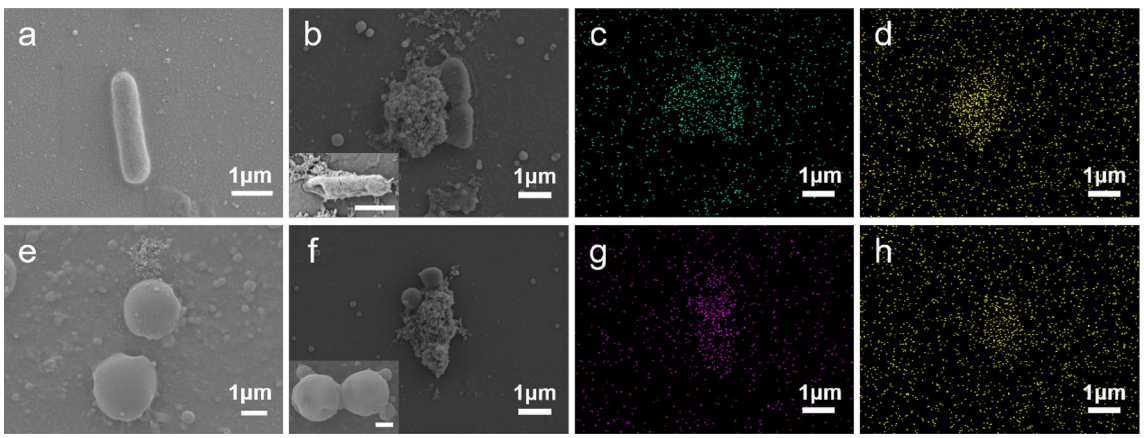

Fig. 10 Images of **a** *E. coli* and **e** *S. aureus*, and images of BSA–Cu_2O antibacterial group after 60 min reaction against *E. coli* (**b** SEM images, **c** elemental mapping of C, **d** elemental mapping of Cu) and *S. aureus* (**f** SEM images, **g** elemental mapping of C, **h** elemental mapping of Cu). The scale of inset is 1 μm

the alkalescent PBS is shown as the following equation [38, 39].

$$Cu_2O + H_2O \rightarrow 2Cu^{+} + 2OH^{-}$$

Compared with other groups (BSA-0–Cu_2O, commercial Cu_2O and CuCl), the amino acid residues of BSA on the surface of BSA–Cu_2O might increase the probability of direct contact with bacteria. It was conducive to increasing the concentration of Cu^{+} in the contact position and releasing Cu^{+} to bacteria.

4 Conclusions

In summary, a novel biomineralization method to fabricate Cu_2O/BSA hierarchical nanocomposite particles is described. Cu_2O/BSA NPS had size of 20–50 nm and were composed of several 6–7 nm Cu_2O nanocrystals and BSA. BSA acted as the structure-directing agent, guiding the formation of Cu_2O/BSA NCPs. N-terminal peptides, histidine and tryptophan residues of BSA coordinated with Cu^{2+} and then controlled the nucleation, growth and assembly of $Cu(OH)_2$ at binding sites to form the hierarchical structure. After the reduction reaction, Cu_2O/BSA NCPs were obtained. The Cu_2O/BSA hierarchical structure exhibited excellent antibacterial performance due to the oriented release of copper ions. The good biocompatibility of BSA was beneficial to the contact with cell walls and site-specific release of Cu^{+}. These findings may be useful for the preparation of hierarchical nanostructures by biomineralization process and application in antibacterial field.

5 Supporting information

The fluorescence spectra and CD spectra of BSA and BSA–Cu_2O. The plate photos of *S. aureus* and *E. coli* cultured with different samples. The FESEM image and XRD pattern of commercial Cu_2O.

Acknowledgements Financial support of this research from the United Innovation Program of Shanghai Commercial Aircraft Engine Fund (AR909), Municipal Bureau of Quality and Technical Supervision Project of Shanghai (2018) is appreciated.

Compliance with ethical standards

Conflict of interest The authors declare that they have no conflict of interest.

References

1. Arivalagan J, Yarra T, Marie B, Sleight VA, Duvernois-Berthet E, Clark MS, Marie A, Berland S (2017) Insights from the shell proteome: biomineralization to adaptation. Mol Biol Evol 34(1):66–77
2. Zeth K, Hoiczyk E, Okuda M (2016) Ferroxidase-mediated iron oxide biomineralization: novel pathways to multifunctional nanoparticles. Trends Biochem Sci 41(2):190–203
3. Wang Z, Huang P, Jacobson O, Wang Z, Liu Y, Lin L, Lin J, Lu N, Zhang H et al (2016) Biomineralization-inspired synthesis of copper sulfide–ferritin nanocages as cancer theranostics. ACS Nano 10(3):3453–3460
4. Kang F, Qu X, Alvarez PJJ, Zhu D (2017) Extracellular saccharide-mediated reduction of Au^{3+} to gold nanoparticles: new insights for heavy metals biomineralization on microbial surfaces. Environ Sci Technol 51(5):2776–2785
5. Wen Y, Dong H, Li Y, Shen A, Li Y (2016) Nano-assembly of bovine serum albumin driven by rare-earth-ion (Gd) biomineralization for highly efficient photodynamic therapy and tumor imaging. J Mater Chem B 4(4):743–751
6. Wang Y, Yang C, Yan X (2017) Hydrothermal and biomineralization synthesis of a dual-modal nanoprobe for targeted near-infrared persistent luminescence and magnetic resonance imaging. Nanoscale 9(26):9049–9055
7. Xie J, Zheng Y, Ying JY (2009) Protein-directed synthesis of highly fluorescent gold nanoclusters. J Am Chem Soc 131(3):888–889
8. Yilmaz E, Ocsoy I, Ozdemir N, Soylak M (2016) Bovine serum albumin-Cu(II) hybrid nanoflowers: an effective adsorbent for solid phase extraction and slurry sampling flame atomic absorption spectrometric analysis of cadmium and lead in water, hair, food and cigarette samples. Anal Chim Acta 906:110–117
9. Mallakpour S, Nazari HY (2017) Ultrasonic-assisted fabrication and characterization of PVC-SiO_2 nanocomposites having bovine serum albumin as a bio coupling agent. Ultrason Sonochem 39:686–697
10. Sasmal AK, Dutta S, Pal T (2016) A ternary Cu_2O–Cu–CuO nanocomposite: a catalyst with intriguing activity. Dalton Trans 45(7):3139–3150
11. Morales-Guio CG, Liardet L, Mayer MT, Tilley SD, Gratzel M, Hu X (2015) Photoelectrochemical hydrogen production in alkaline solutions using Cu_2O coated with earth-abundant hydrogen evolution catalysts. Angew Chem Int Ed 54(2):664–667
12. Selim MS, El-Safty SA, El-Sockary MA, Hashem AI, Elenien OMA, El-Saeed AM, Fatthallah NA (2015) Tailored design of Cu_2O nanocube/silicone composites as efficient foul-release coatings. RSC Adv 5(26):19933–19943
13. Hsu CL, Tsai JY, Hsueh TJ (2016) Ethanol gas and humidity sensors of CuO/Cu_2O composite nanowires based on a Cu through-silicon via approach. Sens Actuator B Chem 224:95–102
14. Yu W, Li F, Wang H, Alarousu E, Chen Y, Lin B, Wang L, Hedhili MN, Li Y et al (2016) Ultrathin Cu_2O as an efficient inorganic hole transporting material for perovskite solar cells. Nanoscale 8(11):6173–6179
15. Emam HE, Ahmed HB, Bechtold T (2017) In-situ deposition of Cu_2O micro-needles for biologically active textiles and their release properties. Carbohydr Polym 165:255–265
16. Shi X, Xue C, Fang F, Song X, Yu F, Liu M, Wei Z, Fang X et al (2016) Full spectrum visible LED light activated antibacterial system realized by optimized Cu_2O crystals. ACS Appl Mater Interfaces 8(13):8386–8392

17. Errokh A, Ferraria AM, Conceicao DS, Ferreira LFV, do Rego AMB, Vilar MR, Boufi S et al (2016) Controlled growth of Cu_2O nanoparticles bound to cotton fibers. Carbohydr Polym 141:229–237
18. Ren J, Wang W, Sun S, Zhang L, Wang L, Chang J (2011) Crystallography facet-dependent antibacterial activity: the case of Cu_2O. Ind Eng Chem Res 50(17):10366–10369
19. Lee YJ, Kim S, Park SH, Park H, Huh YD (2011) Morphology-dependent antibacterial activities of Cu_2O. Mater Lett 65(5):818–820
20. Wang M, Ni Y, Liu A (2017) Investigation on the shape evolution of Cu_2O crystals in the antibacterial process. J Cryst Growth 476:17–24
21. Ma J, Guo S, Guo X, Ge H (2015) Preparation, characterization and antibacterial activity of core–shell Cu_2O@Ag composites. Surf Coat Technol 272:268–272
22. Gao L, Qiu Z, Gan W, Zhan X, Li J, Qiang T (2016) Negative oxygen ions production by superamphiphobic and antibacterial TiO_2/Cu_2O composite film anchored on wooden substrates. Sci Rep 6:26055
23. Li P, Lv W, Ai S (2015) Green and gentle synthesis of Cu_2O nanoparticles using lignin as reducing and capping reagent with antibacterial properties. J Exp Nanosci 11(1):18–27
24. Montazer M, Dastjerdi M, Azdaloo M, Rad M (2015) Simultaneous synthesis and fabrication of nano Cu_2O on cellulosic fabric using copper sulfate and glucose in alkali media producing safe bio- and photoactive textiles without color change. Cellulose 22(6):4049–4064
25. Lee JH (2009) Gas sensors using hierarchical and hollow oxide nanostructures: overview. Sens Actuator B Chem 140(1):319–336
26. Cong L, Xie H, Li J (2017) Hierarchical structures based on two-dimensional nanomaterials for rechargeable lithium batteries. Adv Energy Mater 7(12):1601906
27. Belatik A, Hotchandani S, Carpentier R, Tajmir-Riahi HA (2012) Locating the binding sites of Pb(II) ion with human and bovine serum albumins. PLoS ONE 7(5):e36723
28. Biesinger MC, Lau LWM, Gerson AR, Smart RSC (2010) Resolving surface chemical states in XPS analysis of first row transition metals, oxides and hydroxides: Sc, Ti, V, Cu and Zn. Appl Surf Sci 257(3):887–898
29. Bakare RA, Bhan C, Raghavan D (2014) Synthesis and characterization of collagen grafted poly(hydroxybutyrate-valerate) (PHBV) scaffold for loading of bovine serum albumin capped silver (Ag/BSA) nanoparticles in the potential use of tissue engineering application. Biomacromolecules 15(1):423–435
30. Yang R, Lu X, Huang X, Chen Z, Zhang X, Xu M, Song Q, Zhu L (2015) Bi-component Cu_2O–CuCl composites with tunable oxygen vacancies and enhanced photocatalytic properties. Appl Catal B Environ 170:225–232
31. Boulos SP, Davis TA, Yang J, Lohse SE, Alkilany AM, Holland LA, Murphy CJ (2013) Nanoparticle-protein interactions: a thermodynamic and kinetic study of the adsorption of bovine serum albumin to gold nanoparticle surfaces. Langmuir 29(48):14984–14996
32. Gebregeorgis A, Bhan C, Wilson O, Raghavan D (2013) Characterization of silver/bovine serum albumin (Ag/BSA) nanoparticles structure: morphological, compositional, and interaction studies. J Colloid Interface Sci 389(1):31–41
33. Majorek KA, Porebski PJ, Dayal A, Zimmerman MD, Jablonska K, Stewart AJ, Chruszcz M, Minor W (2012) Structural and immunologic characterization of bovine, horse, and rabbit serum albumins. Mol Immunol 52(3–4):174–182
34. Liang H, Xin B, Wang X (1998) Equilibrium dialysis study on the interaction between Cu(II) and HSA or BSA. Chin Sci Bull 43(5):404–409
35. Zhang Y, Wilcox DE (2002) Thermodynamic and spectroscopic study of Cu(II) and Ni(II) binding to bovine serum albumin. J Biol Inorg Chem 7(3):327–337
36. Meghana S, Kabra P, Chakraborty S, Padmavathy N (2015) Understanding the pathway of antibacterial activity of copper oxide nanoparticles. RSC Adv 5(16):12293–12299
37. Xiong L, Yu H, Nie C, Xiao Y, Zeng Q, Wang G, Wang B, Lv H et al (2017) Size-controlled synthesis of Cu_2O nanoparticles: size effect on antibacterial activity and application as a photocatalyst for highly efficient H_2O_2 evolution. RSC Adv 7(82):51822–51830
38. Wang Y, Gao T, Wang K, Wu X, Shi X, Liu Y, Lou S, Zhou S (2012) Template-assisted synthesis of uniform nanosheet-assembled silver hollow microcubes. Nanoscale 4(22):7121–7126
39. Yang Z, Hao X, Chen S, Ma Z, Wang W, Wang C, Yue L, Sun H et al (2019) Long-term antibacterial stable reduced graphene oxide nanocomposites loaded with cuprous oxide nanoparticles. J Colloid Interface Sci 533:13–23